

## PHYSICAL SCIENCES

# On the nature of decoherence in quantum circuits: Revealing the structural motif of the surface radicals in $\alpha$ -Al<sub>2</sub>O<sub>3</sub>

Sun Un<sup>1\*</sup>, Sebastian de Graaf<sup>2</sup>, Patrice Bertet<sup>3</sup>, Sergey Kubatkin<sup>4</sup>, Andrey Danilov<sup>4</sup>

Quantum information technology puts stringent demands on the quality of materials and interfaces in the pursuit of increased device coherence. Yet, little is known about the chemical structure and origins of paramagnetic impurities that produce flux/charge noise that causes decoherence of fragile quantum states and impedes the progress toward large-scale quantum computing. Here, we perform high magnetic field electron paramagnetic resonance (HF-EPR) and hyperfine multispin spectroscopy on  $\alpha$ -Al<sub>2</sub>O<sub>3</sub>, a common substrate for quantum devices. In its amorphous form,  $\alpha$ -Al<sub>2</sub>O<sub>3</sub> is also unavoidably present in aluminum-based superconducting circuits and qubits. The detected paramagnetic centers are immanent to the surface and have a well-defined but highly complex structure that extends over multiple hydrogen, aluminum, and oxygen atoms. Modeling reveals that the radicals likely originate from well-known reactive oxygen chemistry common to many metal oxides. We discuss how EPR spectroscopy might benefit the search for surface passivation and decoherence mitigation strategies.

## INTRODUCTION

The rise of quantum information science and technology requires ever more coherent devices, and the quality of available materials and interfaces is becoming increasingly important. The charges and spins of unintended surface impurities and defects are sources of fluctuating electric and magnetic fields that can have far-reaching deleterious effects in quantum devices: They set the noise floor in superconducting circuits operating near the quantum sensitivity limit (1–3), including sensors such as superconducting quantum interference devices (4, 5) and photon detectors used for radio astronomy (6), and they induce decoherence in quantum magnetometers (7, 8). In solid-state qubits and quantum circuits, these environmental fluctuators spoil the coherence of the fragile quantum states, thus impeding the progress toward large-scale quantum computing. Although the underlying mechanism is still a matter of wide debate (2, 9–14), surface paramagnetic centers are omnipresent and are considered to be a major contributor to this decoherence. The noise that they induce is largely independent of the specific metals used to fabricate the devices (15), and their surface density in quantum devices (1–3, 11, 16–18) is remarkably constant at about  $10^{17} \text{ m}^{-2}$ .

On-chip electron spin resonance (cESR) is a technique able to directly reveal surface spins present in quantum circuits (18) in situ and to correlate their presence with noise and decoherence (19). However, so far, this technique lacks the resolution to reveal any insightful structural or chemical information about detected spins, particularly for surface radicals on Al<sub>2</sub>O<sub>3</sub> with a  $g_{\text{eff}} \sim 2.0$  ( $g_{\text{eff}} = \hbar\nu/\gamma B_0$ , where  $\nu$  is the measurement frequency and  $B_0$  the corresponding magnetic field). Al<sub>2</sub>O<sub>3</sub> is a material of paramount technological importance as it is a common substrate used for superconducting quantum circuits and it is an archetypical model system for the

surface oxide always present in Al-based superconducting devices (20). While the precise identity and the origin of these surface spins have so far remained elusive, various experiments (13, 21), as well as density functional theory (DFT) calculations (13, 14), have identified physisorbed molecular oxygen as one possible candidate for these noise centers. Less appreciated in this context is that many metal oxides forming in superconducting quantum devices are known to catalyze and stabilize products of one-electron reduction reactions of various molecules, such as superoxide ( $\text{O}_2^-$ ) (22–27). The densities of these surface sites range from  $10^{16}$  to  $10^{18} \text{ m}^{-2}$  in the various polymorphs of Al<sub>2</sub>O<sub>3</sub> (26, 28), comparable to the densities of paramagnetic centers associated with noise in quantum devices. The ability of metal oxide surfaces to promote reactions that form paramagnetic centers raises the question whether the absorbed species are directly responsible for the noise or initiate chemical reactions that create the centers that are. This further complicates the identification of these noise centers and strategies to passivate them.

Here, combining several advanced electron paramagnetic resonance (EPR) spectroscopy techniques together with DFT calculations, we unravel the structure and likely chemical origin of surface radicals on  $\alpha$ -Al<sub>2</sub>O<sub>3</sub>. We argue that the most detrimental surface spins are the result of oxidation of the hydroxylated surface by molecular oxygen. Exploiting the inherently higher resolution of high magnetic field EPR (HF-EPR), we identified three different  $g \sim 2.0$  radical paramagnetic centers in  $\alpha$ -Al<sub>2</sub>O<sub>3</sub> samples prepared and treated in the same manner as the cESR resonators in (18). One of these radicals ( $R_s$ ) could be pinpointed to the surface by its unique proton nuclear magnetic resonance (NMR) spectrum. To acquire the spectrum and to characterize the  $R_s$  nuclear environment, we used high-field electron nuclear double-resonance (ENDOR) and electron double resonance detected nuclear magnetic resonance (ELDOR-NMR) (20). We found that  $R_s$  has a spin density extending across a total of three structurally nonequivalent protons and two aluminum nuclei and the oxygens to which they are bound (Fig. 1D). Key to this finding was the successful application of ELDOR-NMR to detect simultaneous three-spin transitions. Figure 1 shows the conceptual representation of our methods (Fig. 1, A and B) and main findings: The three different

Copyright © 2022  
The Authors, some  
rights reserved;  
exclusive licensee  
American Association  
for the Advancement  
of Science. No claim to  
original U.S. Government  
Works. Distributed  
under a Creative  
Commons Attribution  
NonCommercial  
License 4.0 (CC BY-NC).

<sup>1</sup>Department of Biochemistry, Biophysics and Structural Biology, Institute for Integrative Biology of the Cell, Université Paris-Saclay, CEA, CNRS UMR 9198, Gif-sur-Yvette F-91198, France. <sup>2</sup>National Physical Laboratory, Hampton Road, Teddington TW11 0LW, UK. <sup>3</sup>Quantronics Group, SPEC, CEA, CNRS, Université Paris-Saclay, CEA Saclay, 91191 Gif-sur-Yvette Cedex, France. <sup>4</sup>Department of Microtechnology and Nanoscience, Chalmers University of Technology, SE-41296 Göteborg, Sweden.  
\*Corresponding author. Email: sun.un@cea.fr

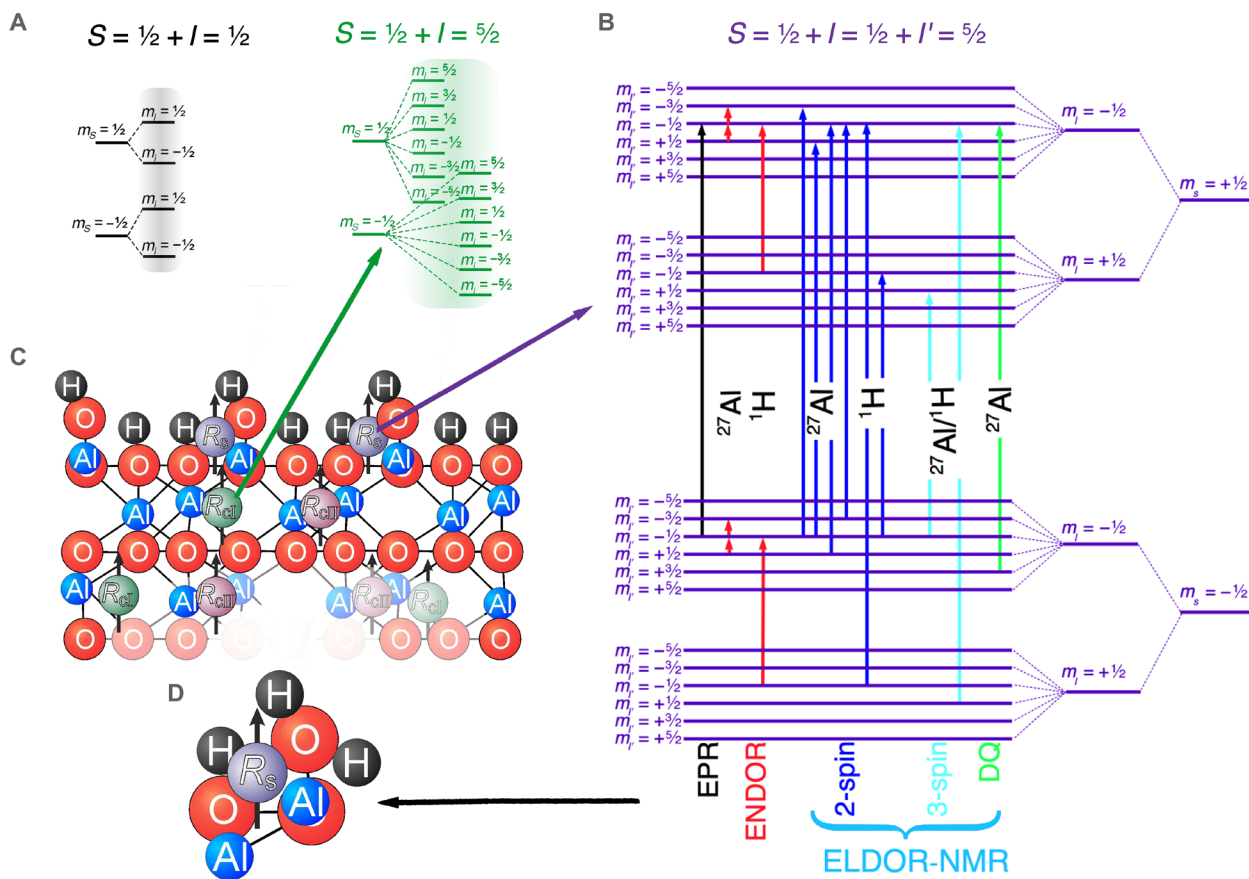


**Fig. 1. Identifying  $\alpha$ - $\text{Al}_2\text{O}_3$  surface radicals by their proximity to proton nuclei.** (A) The trivial energy levels of an electron spin ( $S = 1/2$ ) coupled to a single proton ( $^1\text{H}$ ,  $I = 1/2$ ) and a single aluminum ( $^{27}\text{Al}$ ,  $I = 5/2$ ). (B) The combination of a proton and aluminum nuclei gives rise to a rich set of energy levels. Highlighted are the experimental techniques that we have used to map out these energy levels and reconstruct the environment of radicals. (C) EPR revealed three different radicals in  $\alpha$ - $\text{Al}_2\text{O}_3$ , here sketched near the surface of the  $\text{Al}_2\text{O}_3$  crystal. The NMR spectra of two of the radicals,  $R_{cl}$  and  $R_{cii}$  (green and rose spins), lacked multiple protons in their environment, locating them inside the crystal bulk. By contrast, the NMR spectra of a third radical,  $R_s$ , revealed a coupling to two structurally nonequivalent aluminum and at least three nonequivalent hydrogen atoms, meaning its only possible location would be near the surface. (D) Sketch of the deduced structure of  $R_s$ .

radicals found are depicted as differently colored electrons in Fig. 1C and the complex structure of the surface radical in Fig. 1D.

Through DFT calculations, we further attribute the  $R_s$  formation mechanism to well-documented metal oxide and reactive oxygen reactions. This chemistry is likely to be relevant to all devices based on aluminum Josephson junction technology (29), such as superconducting qubits.

## RESULTS

### HFEPR spectra of $\alpha$ - $\text{Al}_2\text{O}_3$

Three different  $\alpha$ - $\text{Al}_2\text{O}_3$  radical centers, which we will refer to as  $R_{cl}$ ,  $R_{cii}$ , and  $R_s$ , were identified by HFEPR (Fig. 2).  $R_{cl}$  and  $R_{cii}$  are located inside the crystal and will be described in detail in a future communication. Here, we focus on  $R_s$ , which, we will demonstrate, are localized on the surface. The  $R_s$  spectrum was readily evident at 285 GHz (10 T) and 190 GHz (6 T) (Fig. 2A). It was centered at a  $g_{\text{eff}}$  of 2.0065 with a width of 7 mT at 285 GHz. By contrast,  $R_s$  was not apparent in the 94-GHz (3-T) spectra, which were detected using the pulse Hahn spin-echo sequence (fig. S2) (30). The specific conditions of these measurements ensured that these 94-GHz spectra

correctly reflected the contributions of  $R_{cl}$ ,  $R_{cii}$ , and  $R_s$ . By comparison, the conventional continuous-wave excitation method used to obtain the 190- and 285-GHz spectra limited us to conditions where the contributions of the three radical species became dependent on their spin relaxation (see Materials and Methods) that apparently enhanced the contribution of  $R_s$ . By appropriately choosing the timing of the Hahn echo pulses, we were able to differentiate the radical species based on their spin relaxation and isolate the spectrum of  $R_s$  because of its faster spin relaxation (Fig. 2C). These data show that the actual contribution of  $R_s$  was 3 to 10% of the total radical population. The isolated spectra of  $R_s$ , unlike those of  $R_{cl}$  and  $R_{cii}$ , only weakly depend on the crystal orientation with respect to the applied magnetic field,  $B_0$  ( $\theta_{cB_0}$ , fig. S1); that is, the anisotropy in the  $g$  value of  $R_s$  is likely to be small. This and its faster relaxation suggest that  $R_s$  has a significantly different structure and environment from those of the other two radicals.

The width of the  $R_s$  EPR spectrum is also essentially independent of the observation frequency: 6 mT at 94 GHz and 7 mT at 285 GHz (Fig. 2A). This demonstrates that the shapes of the  $R_s$  EPR spectra are dominated by small unresolved field-independent spin-spin interactions. The largest of these are expected to be the magnetic

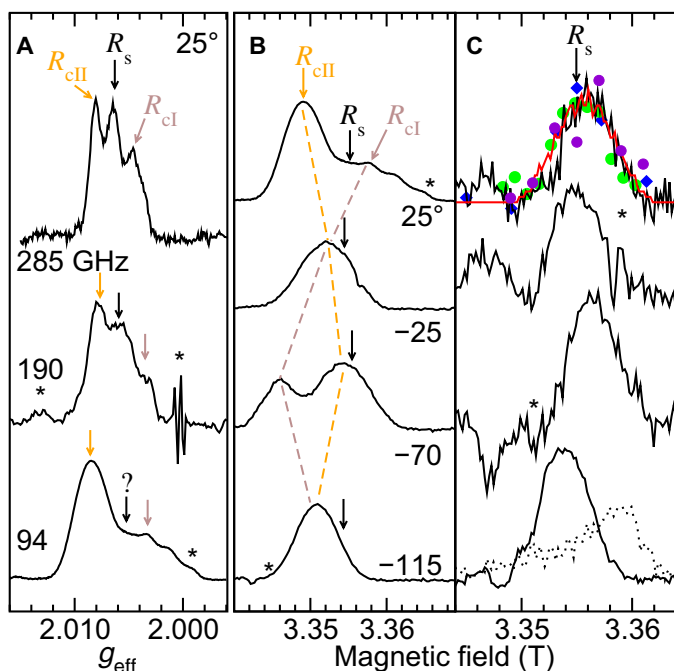


**Fig. 2. Three distinct  $\alpha$ - $\text{Al}_2\text{O}_3$  radicals are revealed by HFEPR.** (A) The HFEPR spectra of  $\alpha$ - $\text{Al}_2\text{O}_3$  at 94-, 190-, and 285-GHz microwave frequencies with the applied magnetic field,  $B_0$ , oriented  $25^\circ$  with respect to the crystal  $c$  axis ( $\theta_{cB_0} = 25^\circ$ ). The 190- and 285-GHz spectra were obtained using conventional continuous-wave excitation and the 94-GHz spectra using a two-pulse spin-echo scheme (fig. S2 and Materials and Methods for details). The 190- and 285-GHz spectra reveal three distinct radicals:  $R_s$ ,  $R_{cl}$ , and  $R_{cll}$ . (B) The 94-GHz spectra taken at various  $\theta_{cB_0}$  about the crystal  $a$  axis.  $R_{cl}$  and  $R_{cll}$  show distinct orientation dependences indicated by the brown and orange dashed lines, but the contribution of  $R_s$  is not apparent in any of these spectra. (C) The isolated 94-GHz spectra of  $R_s$ . The spectra of  $R_s$  are only weakly  $\theta_{cB_0}$  dependent and centered at a  $g_{\text{eff}}$  of 2.0065 ( $B_0 = 3.3550$  T at 94 GHz). The black arrows in (B) indicate the position of  $R_s$ . A contribution from the microwave cavity of the 94-GHz spectrometer (dotted trace) has been subtracted from the spectra in (C). Superimposed on these spectra are the following: blue diamonds indicating the amplitudes of the  $^1\text{H}$  ELDOR-NMR detected EPR spectra of the  $\text{H}_M$  protons; violet and green circles respectively indicating the amplitudes of the  $^{27}\text{Al}$  ENDOR detected EPR spectra of  $\text{Al}_{12}$  and  $\text{Al}_5$  in Fig. 4B and C; and a simulation (red) based on the  $R_s$   $^{27}\text{Al}$  and  $^1\text{H}$  hyperfine couplings measured by ELDOR-NMR and ENDOR (see text and the Supplementary Materials for details). All these results are in very good agreement with the measured HFEPR data for  $R_s$ .

interactions between the unpaired electron and nuclear spins of aluminum atoms and, if present, hydrogen atoms. We now turn to the characterization of these hyperfine interactions.

### The structure of $R_s$ and its localization

The size of such hyperfine interactions,  $A$ , reveals details about the distance between the electron and nuclei, the nature of their chemical bonding, and their mutual orientation with respect to  $B_0$ . To gain insights into the electronic structure of the  $R_s$  centers, we measured these interactions by obtaining the NMR spectra of the  $R_s$  nuclei using 94-GHz Davies pulsed ENDOR (31) and ELDOR-NMR (20) spectroscopy. The  $^1\text{H}$  ELDOR-NMR spectra are shown in Fig. 3. Three protons,  $\text{H}_{16}$ ,  $\text{H}_{25}$ , and  $\text{H}_{40}$ , are identifiable by their effective nominal hyperfine couplings,  $|A_{\text{eff}}|$ , of 32, 50, and 80 MHz, respectively (Fig. 3A). There was also a fourth resonance around 0 MHz, arising from small couplings ( $<8$  MHz) characteristic of nuclei in

the environment (“matrix”) surrounding the radical. The complex shape of this resonance (Fig. 3B) indicates that it arose from more than one proton, which we designate  $\text{H}_M$ . We were able to unambiguously link this ELDOR-NMR-detected matrix resonance to  $R_s$  by matching its field-dependent amplitude (Fig. 3C) to the EPR spectrum of  $R_s$  (Fig. 2C and fig. S3). This also established that  $R_s$  had a number of protons in its environment, indicating that it was a surface species (see below). The aluminum body of the microwave cavity of the HFEPR spectrometer itself contributed smaller  $^1\text{H}$  resonances similar to those from  $\alpha$ - $\text{Al}_2\text{O}_3$ . These likely originate from hydrated aluminum oxide that coats the aluminum metal, meaning that the same radical is likely present on the amorphous oxide of any Al surface.

Having characterized the proton environment of  $R_s$ , we now turn to the hyperfine coupling of  $R_s$  to  $^{27}\text{Al}$  using ENDOR. The  $^{27}\text{Al}$  ENDOR spectra of  $R_s$ ,  $R_{cl}$ , and  $R_{cll}$  were similar (Fig. 4A). This suggested that the three different centers shared common electronic structural motifs. The  $B_0$  dependence of ENDOR resonances (i.e., the  $^{27}\text{Al}$  ENDOR-detected EPR spectra) of two aluminum atoms, designated  $\text{Al}_5$  and  $\text{Al}_{12}$ , was identical to the  $R_s$  EPR spectrum (Fig. 4, B and C, and fig. S4). The sharpness of these two ENDOR resonances (full width at half-height of less than 75 kHz) indicated that their hyperfine and nuclear quadrupolar interactions had little or no radical-to-radical variation. From this, we concluded that the  $R_s$  centers were structurally well defined because hyperfine interactions are known to be sensitive to the structure and local environments of the nuclei (32).

### Correlating multiple nuclei to the same $R_s$ center

After mapping the individual hyperfine interactions and identifying the  $^1\text{H}$  and  $^{27}\text{Al}$  nuclei associated with  $R_s$ , we next turn to understanding whether the detected atoms belong to the same  $R_s$  radical. Using ELDOR-NMR, we measured the spectra of three-spin transitions that involve the simultaneous flipping of the electron spin of the radical and two nuclear spins, typified by the cyan transitions in Fig. 1B. (By contrast, conventional two-spin ELDOR-NMR spectra like those in Fig. 3 arise from flipping the spins of the electron and only one nucleus illustrated by the blue transitions in Fig. 1B.) The three-spin transitions are only possible when both nuclear spins are coupled to the same electron spin center. A quantitative treatment of the three-spin ELDOR-NMR is given in the Supplementary Materials. In the following, we summarize the salient results.

Three-spin resonances occur at the sums (illustrated by the right cyan arrow in Fig. 1) and differences (left cyan arrow) of the frequencies of the two individual nuclear spins. These two-spin frequencies are the same as the ones measured by  $^{27}\text{Al}$  ENDOR and two-spin  $^1\text{H}$  ELDOR-NMR. The three-spin spectra at the sum frequencies are shown in Fig. 5 (A to C) along with their corresponding two-spin spectra. Superimposed on these spectra are some of the pairwise sums of the individual frequencies of  $\text{H}_{16}$ ,  $\text{H}_{25}$ ,  $\text{H}_{40}$ ,  $\text{H}_M$ ,  $\text{Al}_5$ ,  $\text{Al}_{12}$ , and  $\text{Al}_M$  obtained from Figs. 3 and 4. The three-spin spectra have unmistakable intensities at these calculated frequencies, for example, at the frequencies labeled “ $\text{Al}_M + \text{H}_{16}$ ,” “ $\text{Al}_M + \text{H}_{25}$ ,” and “ $\text{Al}_M + \text{H}_{40}$ ” in the region highlighted in gray in Fig. 5B. The presence of three-spin resonances at these three particular frequencies along with those at “ $\text{H}_M + \text{H}_{16}$ ,” “ $\text{H}_M + \text{H}_{25}$ ,” and “ $\text{H}_M + \text{H}_{40}$ ” demonstrates that each of the  $\text{H}_{16}$ ,  $\text{H}_{25}$ , and  $\text{H}_{40}$  nuclei is associated with not only at least one  $\text{Al}_M$  atom but also at least one  $\text{H}_M$  atom. Such nuclear spin correlations can be extended by considering the

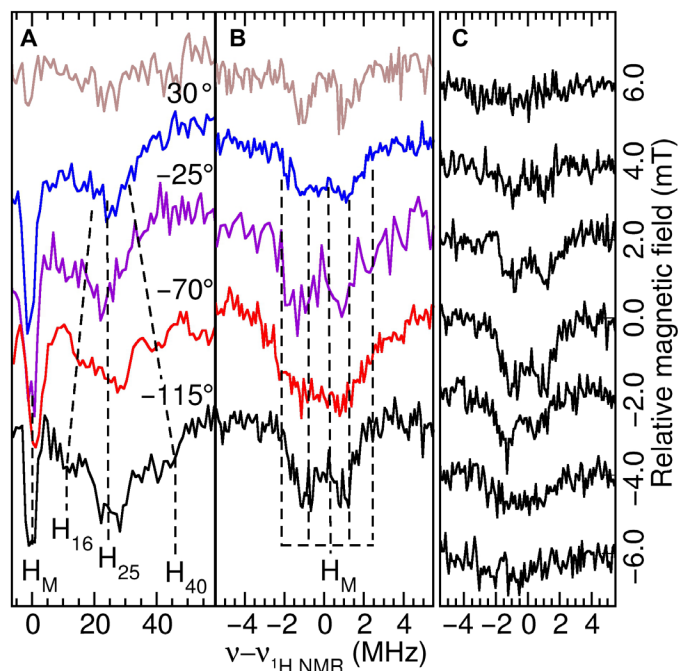


**Fig. 3. Protons are integral to the structure and environment of  $R_s$ .** (A) The 94-GHz  $^1\text{H}$  ELDOR-NMR spectra of  $\alpha\text{-Al}_2\text{O}_3$  measured at four different orientations  $\theta_{cB_0}$  at the magnetic field  $B_0$  corresponding to the maximum of the  $R_s$  EPR spectrum ( $g = 2.0065$ ). Four different  $R_s$  protons,  $\text{H}_{40}$ ,  $\text{H}_{25}$ ,  $\text{H}_{16}$ , and  $\text{H}_M$ , are apparent, with a hyperfine coupling  $A$  of 86, 50, 22, and 0 MHz, respectively (A corresponds to twice the relative resonance frequencies). The brown traces are the spectra arising from the spectrometer microwave cavity. The frequency scales are relative to the microwave detection frequency (94 GHz) and the  $^1\text{H}$  NMR(Zeeman) frequency ( $\nu_{^1\text{H,NMR}} = \gamma_{^1\text{H}}B_0$ , where  $\gamma_{^1\text{H}}$  is the magnetogyric ratio of the proton). (B) The expanded detailed view of the  $\text{H}_M$  resonances. The partially resolved line shapes and their orientation dependence indicate that  $\text{H}_M$  is a collection of protons with  $|A_{\text{eff}}| < 8$  MHz. (C) The  $B_0$  dependence of the  $\text{H}_M$  resonances relative to 3.3550 T ( $g = 2.0065$ ) for  $\theta_{cB_0} = -115^\circ$ . ELDOR-NMR-detected EPR spectrum (Fig. 2C, blue diamonds) constructed from these data matches the spectrum of  $R_s$ .

blue  $^1\text{H}/^1\text{H}$  region in Fig. 5C. Intensities at the frequencies corresponding to “ $\text{H}_{16} + \text{H}_{25}$ ” and “ $\text{H}_{25} + \text{H}_{40}$ ” show that these three nuclei reside together on a common center. Furthermore, the frequencies covered by the  $^{27}\text{Al}/^{27}\text{Al}$  and  $^{27}\text{Al}/^1\text{H}$  blue regions match other pairwise sums of resonance frequencies; for example, in Fig. 5A, the sum of  $\text{Al}_5$  and  $\text{Al}_{12}$  at 17 MHz and, in Fig. 5B, the sum of  $\text{Al}_{12}$  and  $\text{H}_{40}$  at 52 MHz.

In summary, we were able to identify enough pairwise correlations to establish that  $\text{H}_{16}$ ,  $\text{H}_{25}$ ,  $\text{H}_{40}$ ,  $\text{H}_M$ ,  $\text{Al}_5$ ,  $\text{Al}_{12}$ , and  $\text{Al}_M$  all belong to a common  $R_s$  center. Figure 5D graphically summarizes the extended structure of  $R_s$  as revealed from the three-spin data. Here, we have drawn the pairwise correlations deduced from Fig. 5 (A to C) as solid lines. The arrangement of the nuclei is based on the DFT calculations described below.  $\text{H}_M$  arises from multiple hydrogen atoms that surround  $R_s$ . Because such an environment with a large number of protons is unique only to the hydrated and hydroxylated surface of the  $\alpha\text{-Al}_2\text{O}_3$  crystal,  $R_s$  could unambiguously be identified as surface centers. Furthermore, simulations of the  $\theta_{cB_0} = 25^\circ$   $R_s$  EPR spectrum based on the  $\text{H}_{16}$ ,  $\text{H}_{25}$ ,  $\text{H}_{40}$ ,  $\text{Al}_5$ , and  $\text{Al}_{11}$  hyperfine couplings were able to reproduce the  $R_s$  EPR spectrum in its

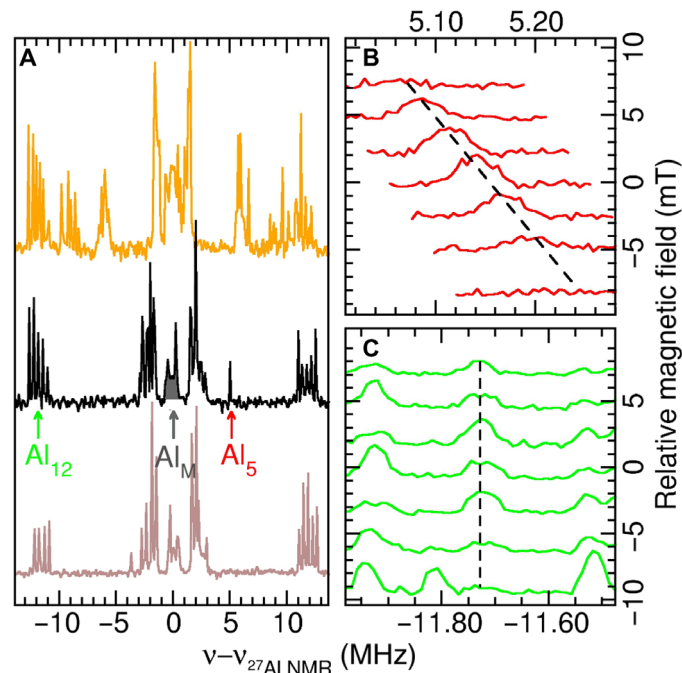


**Fig. 4.  $R_s$  has two distinct aluminum atoms in its structure.** (A) The 94-GHz  $\theta_{cB_0} = 25^\circ$  Davies  $^{27}\text{Al}$  ENDOR spectra of  $\alpha\text{-Al}_2\text{O}_3$ . ENDOR traces were obtained at the magnetic fields indicated by the correspondingly colored arrows in Fig. 2A. These are the positions where the spectra of  $R_s$  (black) and the bulk radicals,  $R_{\chi 1}$  (orange) and  $R_{\chi 2}$  (brown), reach their respective maxima. The frequency scales are relative to the  $^{27}\text{Al}$  NMR(Zeeman) frequency ( $\nu_{^{27}\text{Al,NMR}} = \gamma_{^{27}\text{Al}}B_0$ ). (B and C) The magnetic field dependence (relative 3.3550 T or  $g = 2.0065$ ) of the two  $R_s$  aluminum hyperfine resonances,  $\text{Al}_5$  (red) and  $\text{Al}_{12}$  (green), respectively. The associated  $^{27}\text{Al}$  ENDOR-detected EPR spectrum that matches the EPR spectrum of  $R_s$  is shown in Fig. 2C. The gray shaded region ( $\text{Al}_M$ ) arises from matrix  $^{27}\text{Al}$  nuclei that experience small hyperfine interactions and are in the environment of the radical centers.

entirety (Fig. 2C, red trace). These same spin interactions also reproduced the cESR spectra (18). From this, we concluded that these five atoms and the oxygens to which they were bound defined  $R_s$  and that the unpaired electron spin density was delocalized over this group of atoms.

### Surface density of $R_s$ is similar to that of surface spins in quantum circuits

Using TEMPO ((2,2,6,6-tetramethylpiperidin-1-yl)oxyl), a stable organic radical, as a concentration standard, we determined the total concentration of radical centers in  $\alpha\text{-Al}_2\text{O}_3$  (Fig. 2B) to be about  $3 \times 10^{22} \text{ m}^{-3}$ .  $R_s$  constituted 3 to 10% of this total, corresponding to a surface spin density of 1 to  $3 \times 10^{17} \text{ m}^{-2}$ . This is comparable to the abundance of chemically catalytic “electron donor” sites found in other polymorphs of  $\text{Al}_2\text{O}_3$  (26, 28) and also the  $g_{\text{eff}} = 2$  surface spin density detected in  $\alpha\text{-Al}_2\text{O}_3$  by cESR measurements (18) and agrees with the surface density of paramagnetic centers, accounting for the magnetic noise observed in superconducting circuits (1, 2, 11, 17, 18, 33). On the basis of this density and the consistency between HFEPR and cESR spectra, we concluded that the  $g_{\text{eff}} = 2$  species detected by cESR and the  $R_s$  centers detected by HFEPR were one in the same, the surface centers associated with the associated with the flux and charge noise in the superconducting cESR resonators (18, 34).



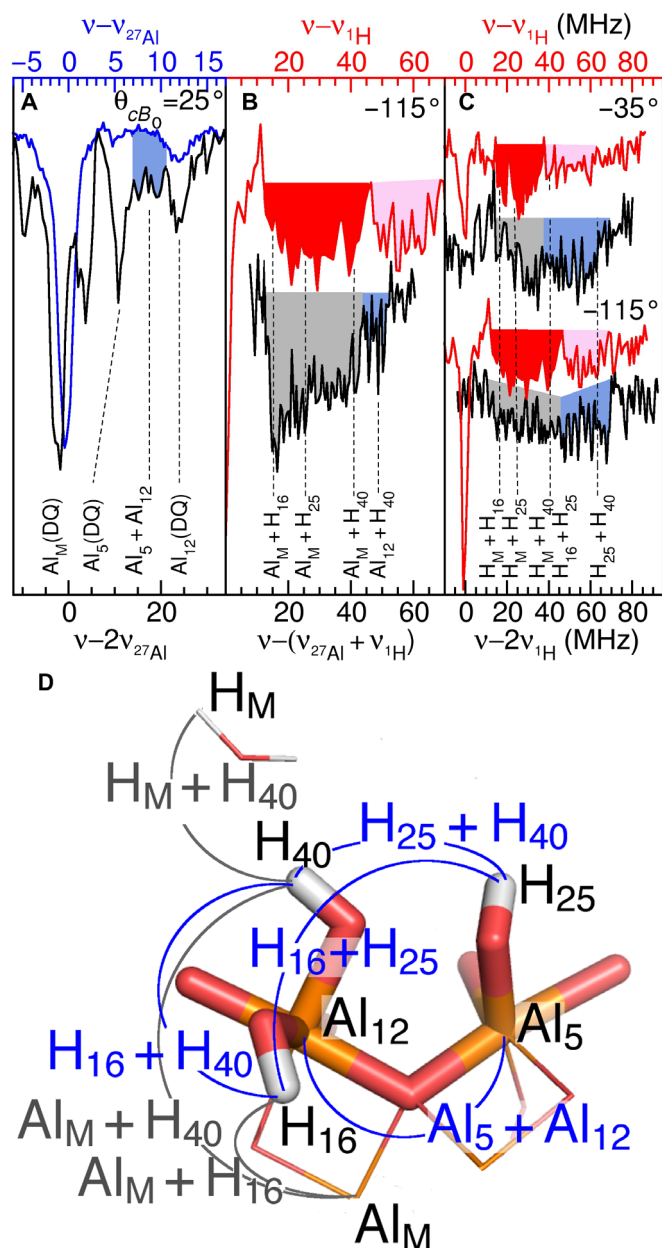


**Fig. 5. Three-spin ELDOR-NMR demonstrates that the detected aluminum and proton nuclei reside on a common  $R_5$  center.** (A) The three-spin  $^{27}\text{Al}/^{27}\text{Al}$ , (B)  $^{27}\text{Al}/^1\text{H}$ , and (C)  $^1\text{H}/^1\text{H}$  regions of the ELDOR-NMR spectra. The frequency scales of the three-spin spectra (black) are relative to their respective sum of NMR (Zeeman):  $2\nu_{^{27}\text{Al,NMR}}$ ,  $\nu_{^{27}\text{Al,NMR}} + \nu_{^1\text{H,NMR}}$ , and  $2\nu_{^1\text{H,NMR}}$  and the two-spin spectra (blue and red traces and frequency scales) relative to their corresponding simple NMR (Zeeman) frequencies. The gray highlights the three-spin regions that span the same frequencies as the two-spin frequencies of  $\text{H}_{16}$ ,  $\text{H}_{25}$ , and  $\text{H}_{40}$  (shaded in red). The blue regions indicate three-spin transitions that have no corresponding resonances in the two-spin spectra, indicating that these arise from three-spin transitions of pairwise combinations of  $\text{H}_{16}$ ,  $\text{H}_{25}$ ,  $\text{H}_{40}$ ,  $\text{Al}_5$ , and  $\text{Al}_{12}$ . The pink areas indicate three-spin  $^{27}\text{Al}/^1\text{H}$  transitions visible in the two-spin spectra. The dashed lines and labels show the sum of the frequencies of two-spin transitions established by ENDOR and ELDOR-NMR. (D) The network of connected nuclei reconstructed from the spectra superimposed on a model of  $R_5$ . A water molecule has been included in the model to represent the interactions between  $R_5$  and the hydration layer that covers the  $\alpha\text{-Al}_2\text{O}_3$  surface. Connections to the  $\text{Al}_M$  and  $\text{H}_M$  are only illustrative; many other distant interactions with surrounding  $^{27}\text{Al}$  and  $^1\text{H}$  nuclei could be involved. See Computational modeling of  $R_5$  to reveal its structure and the Supplementary Materials for more details.

### Computational modeling of $R_5$ to reveal its structure

We combined the magnetic resonance measurements on  $R_5$  with DFT calculations to model its structure. These calculations used hypothetical neutral  $\text{Al}_8\text{O}_{30}\text{H}_{36}$  nanoparticles. Their structures were based on the  $\alpha\text{-Al}_2\text{O}_3$  unit cell ( $\text{Al}_8\text{O}_9$ ) and experimental studies of the  $\alpha\text{-Al}_2\text{O}_3$ -water interface that showed that the exposed aluminum atoms were fully terminated with oxygens from water and hydroxyl groups (Fig. 6, fig. S6, and the Supplementary Materials) (35). Although these models did not capture the crystalline nature of  $\alpha\text{-Al}_2\text{O}_3$  and were far from exhaustive in terms of the different possible geometries of the terminal hydroxylated aluminum and aluminum oxide groups on the  $\alpha\text{-Al}_2\text{O}_3$  surface, they did allow for adequate prediction of atomic-level properties, such as spin and charge distributions and bonding interactions. This provided a means for modeling and examining the possible interactions and reactions between  $\text{O}_2$  and the  $\alpha\text{-Al}_2\text{O}_3$  surface that are thought to be important in the creation of noise centers (13, 14, 21) and, at the same time, the ability to calculate the EPR properties of the resulting molecular complexes and products. Of particular interest were the radical centers that were formed and that could serve as structural models of  $R_5$ . To ensure that the DFT methods had predictive value, we first confirmed that they were able to compute, with reasonable accuracy, the  $g$  values and hyperfine interactions of other previously studied aluminum-based radicals (see the Supplementary Materials). Having established this, we applied them to the  $\text{Al}_8\text{O}_{30}\text{H}_{36}$  nanoparticles and compared the calculated  $g$  values and hyperfine couplings to those measured for  $R_5$  to identify which structural motifs had compatible values. In this way, we are able to derive a model of the structure of  $R_5$ .

For most cases where an  $\text{O}_2$  molecule was placed within 1.8 Å of the nanoparticle, geometry optimization led to structures that resembled physisorbed oxygen in which the two molecules only weakly interacted, as depicted in 1 (Fig. 6 and fig. S6B). The triplet character remained on  $\text{O}_2$ , and the charge distribution was similar to the individual neutral molecules. However, for certain  $\text{O}_2$  orientations and distances, geometry optimization resulted in a hydrogen atom transfer to the  $\text{O}_2$  molecule resembling 2 (Fig. 6 and fig. S6A), forming a final structure that resembled a  $\text{HO}_2^{\cdot}[\text{Al}_8\text{O}_{30}\text{H}_{35}]^{\cdot}$  radical pair. Its calculated  $g$  and hyperfine values were similar to those of superoxide on  $\gamma\text{-Al}_2\text{O}_3$  (see below).

By contrast, the isolated  $[\text{Al}_8\text{O}_{30}\text{H}_{35}]^{\cdot}$  nanoparticle radicals had  $g$  and hyperfine values similar to the measured values for  $R_5$ . The calculated  $^{27}\text{Al}$  hyperfine interactions of these radicals depended on the protonation state of the oxygen atoms surrounding the aluminum atoms (Fig. 6 and fig. S6). In general, the more polarized complexes had larger hyperfine interactions. One aluminum atom in radical 3 is surrounded by three hydroxide ligands and an adjacent aluminum atom by two. Most of the unpaired spin density rests on three of the oxygen atoms bound to these two atoms. The calculated isotropic or average  $^{27}\text{Al}$  hyperfine couplings of these two aluminum nuclei are  $-19$  and  $-9$  MHz, in good agreement with the measured values of  $\text{Al}_5$  and  $\text{Al}_{12}$ . This was also true for the anisotropic, or the orientation-dependent, components of these hyperfine couplings (fig. S4E) which calculations predict are small, 2 MHz. The agreement between calculations and measurements also extends to the two large  $-87$ - and  $-55$ -MHz  $^1\text{H}$  hyperfine couplings that were comparable to the absolute values of 84 and 50 MHz measured by ELDOR-NMR for  $\text{H}_{40}$  and  $\text{H}_{25}$  (Fig. 3A). Given this consistency and the sensitivity of the  $^1\text{H}$  and  $^{27}\text{Al}$  hyperfine interactions to the details of the unpaired electron spin distribution, we conclude

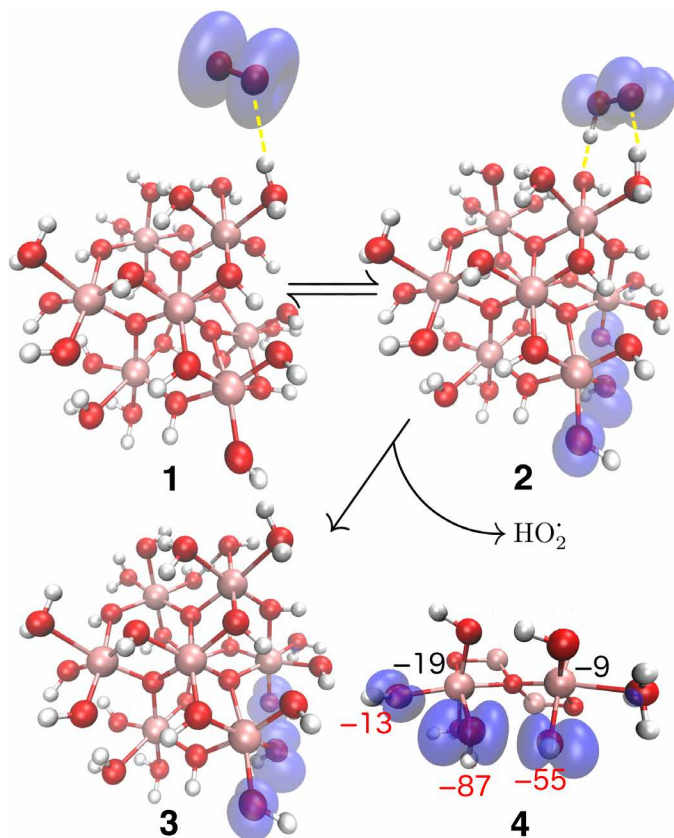


**Fig. 6. Interactions between  $O_2$  and  $\alpha\text{-Al}_2O_3$  surface can lead to outer-sphere electron transfer and radical formation.** DFT studies of the interactions between  $O_2$  and neutral  $Al_3O_3H_36$  nanoparticle models of the  $\alpha\text{-Al}_2O_3$  surface show that the most common interactions are those similar to structure **1**, modeling physisorbed  $O_2$  on  $\alpha\text{-Al}_2O_3$ . However, geometry optimization of certain initial configurations leads to a hydrogen atom transfer from the nanoparticle to the  $O_2$  forming radical pairs similar to **2**. Structure **3**, obtained by reoptimizing the structure of **2** with the protonated superoxide removed, leads to a radical with calculated hyperfine couplings that closely resembled those measured for  $R_s$ . Structure **4** is a simplified view of the radical center in **3**. The blue surfaces depict the distribution of the unpaired electron spin density. The calculated average (or isotropic) hyperfine interactions experienced by the two  $^{27}Al$  nuclei are indicated in black in megahertz, and the largest component experienced by the protons is in red.

that the structure of  $R_s$  resembles **4**, the  $[Al(OH)_3\text{-O-Al(OH)}_2(H_2O)]$  radical center. The calculated isotropic  $g$  value of this structure is 2.0060, which matched the  $R_s$  value of 2.0065. However, the anisotropy in  $g$  is predicted to range from 2.0086 to 2.0024, greater than observed for  $R_s$  based on its HFEPR spectra (Fig. 2B).

### Surface reactions with reactive oxygen species: Long-term stability of $R_s$

The sequence of structures in Fig. 6 depicts oxidation of the nanoparticle by a weakly interacting oxygen molecule, commonly known as an “outer-sphere” electron transfer reaction (19). The formation of  $R_s$  by oxidation of the  $\alpha\text{-Al}_2O_3$  surface is consistent with the known chemistry of a variety of metal oxides that undergo surface oxidation by molecular oxygen and stabilized radical centers on their surfaces (22–28). If this were the case, the surface density of  $R_s$  may represent a steady-state population that is not necessarily static and is

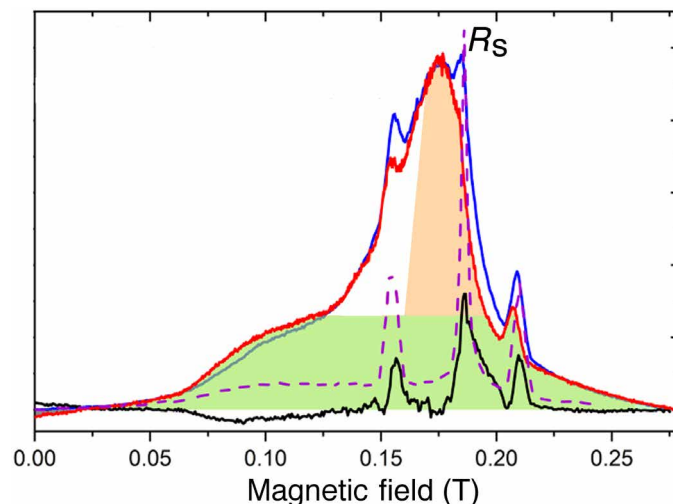


**Fig. 7. Argon/ $O_2$  plasma treatment leads to long-term reduction in  $R_s$ .** cESR spectra (5.0 GHz) of the  $\alpha\text{-Al}_2O_3$  surface of the superconducting cESR microwave resonator: before treatment (dashed purple), after treatment with  $O_2$  plasma followed by exposure to water (blue), and the same sample 4.5 years after treatment (red). The black trace shows what is lost after 4.5 years. The green region corresponds to contribution from triplet  $O_2$ , and the orange region denotes where contributions from superoxides ( $O_2^-$  and  $HO_2^-$ ) are expected. The peak at 0.185 T arises from  $R_s$ . The two narrow flanking resonances are from atomic H, which have been removed in the samples used in this study.

affected by shifts in concentrations of the  $O_2$  and superoxides. We have found indications of this in recent measurements of the Ar/ $O_2$  plasma-treated cESR microwave resonator used in a previous study (Fig. 7) (18). Plasma treatment of the  $\alpha\text{-Al}_2O_3$  surface of these resonators followed by exposure to water had no net initial effect on  $R_s$  (Fig. 7, blue trace) (18). Given its  $\sim 150\text{-eV}$  energy, the plasma likely destroyed  $R_s$ , which re-formed afterward. In addition to  $R_s$  and atomic H, the cESR spectrum of the plasma-treated  $\alpha\text{-Al}_2O_3$  showed a marked increase in the very broad  $O_2$ -like component and the appearance of a large resonance consistent with superoxides (Fig. 7) (18, 34). The  $O_2$  plasma in the presence of water produces  $O_2$ , ozone, hydroxide radicals ( $HO^\bullet$ ), peroxide, and superoxides (36, 37). Of these, the  $HO^\bullet$  radicals are extremely reactive, and their lifetime on the surface is expected to be short. The surface densities of the paramagnetic species created by the plasma were stable and, based on the amplitudes of their EPR resonances, significantly greater than that of  $R_s$ . Evidently, their presence affected neither the densities nor the EPR spectrum of  $R_s$  or atomic hydrogen, suggesting that they were physically separated from the plasma-induced species. Recurrent measurements on the same samples show that  $R_s$  and hydrogen had significantly diminished over 4 years (Fig. 7). By comparison, the spectra of  $R_s$  in untreated samples remained constant over similar lengths of time. This demonstrated that the population of  $R_s$  is not static and is affected by the presence of the plasma-induced species, most likely one or more of the abundant oxygen species. The slowness of these changes reinforces the hypothesis that these species were physically partitioned from  $R_s$ .

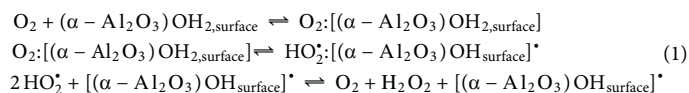
### DISCUSSION

It has been proposed that a possible source of flux and charge noise in quantum devices is physisorbed molecular oxygen ( $O_2$ ) (13, 14, 21, 34).

Our results do not support this interpretation. O<sub>2</sub> molecules weakly interacting with the α-Al<sub>2</sub>O<sub>3</sub> surface would retain their triplet state character (similar to Fig. 6A). DFT calculations on the interaction of O<sub>2</sub> with the [Al<sub>8</sub>O<sub>30</sub>H<sub>35</sub>]<sup>•</sup> nanoparticle model demonstrate this. In this case, the EPR of the α-Al<sub>2</sub>O<sub>3</sub> surface would be dominated by a very broad resonance extending from  $g_{\text{eff}} \sim 4$  to low values, owing to the large magnetic anisotropy of O<sub>2</sub> arising from their zero-field interaction of 100 GHz (38). This matches the very broad underlying resonance seen in the cESR spectra (Fig. 7, green region). In contrast to this wide O<sub>2</sub> background, the cESR (and HFEPR) spectra of the species identified as the noise sources are very narrow. The spectrum of R<sub>s</sub> is much narrower than those of superoxides (O<sub>2</sub><sup>•-</sup> and HO<sub>2</sub><sup>•</sup>) (23). A typical EPR spectrum of superoxide on the surface of γ-Al<sub>2</sub>O<sub>3</sub> spans 2.07 to 2.04 to 2.00 in  $g_{\text{eff}}$ , corresponding to the orange region in Fig. 7. Their <sup>27</sup>Al hyperfine interactions are less than 500 kHz (27), significantly smaller than those of R<sub>s</sub>. In general, we do not expect physisorbed paramagnetic species to have substantial <sup>27</sup>Al hyperfine interactions, particularly ones with large average or isotropic values, like those of R<sub>s</sub>, because these are indicative of covalent bonding.

The HFEPR measurements show that R<sub>s</sub> is a very stable and structurally well-defined radical center immanent to the α-Al<sub>2</sub>O<sub>3</sub> surface. The DFT calculations suggest that R<sub>s</sub> are specific to particular hydroxylated aluminum oxide sites on the crystal surface resembling structure 4 in Fig. 6. Similar radical centers are apparently not unique to α-Al<sub>2</sub>O<sub>3</sub>. The aluminum resonator used for HFEPR measurements also had stable paramagnetic centers with similar HFEPR (Fig. 2) and <sup>1</sup>H ELDOR-NMR spectra (Fig. 3). These centers are most likely located on the aluminum oxide layer that forms on the metal surface due to oxidation. If this is the case, it is reasonable to assume that all devices using aluminum structures have such similar stable radicals on their surfaces. As is evident from our findings, unlike atoms and molecules physisorbed onto α-Al<sub>2</sub>O<sub>3</sub>, R<sub>s</sub> cannot be physically removed because they are integral to the α-Al<sub>2</sub>O<sub>3</sub> surface; they must be chemically “silenced” instead.

Formation of R<sub>s</sub> should also lead to detectable amounts of superoxide radicals, which are stable. Superoxides on metal oxide surfaces are readily detectable by EPR (22), but none were detected by HFEPR on our samples of α-Al<sub>2</sub>O<sub>3</sub>, and, so far, only suggested as a plausible alternative to molecular oxygen to explain cESR (18) measurements, which lacked sufficient sensitivity to resolve specific details. We attribute this lack of superoxide signal to the fact that they are capable of undergoing disproportionation reactions, leading to peroxide and molecular oxygen (39). The former is not paramagnetic, and the latter, as discussed above, has an EPR spectrum that is significantly broader than that of superoxides. Hence, disproportionation would leave R<sub>s</sub> as the only readily EPR detectable species. The overall mechanism for the formation of R<sub>s</sub> in this case is given by



Implicit to this scheme is that superoxides can diffuse freely on the surface. The aqueous layer physisorbed over the α-Al<sub>2</sub>O<sub>3</sub> surface may play an important role in facilitating this movement. It may also provide a protective barrier for R<sub>s</sub>, thus enhancing its stability. R<sub>s</sub> and atomic hydrogen can be removed with 300°C heating under vacuum. Hydrogen can be readily taken off while R<sub>s</sub> appears to be

significantly more robust and persistent. The density of aluminum hydroxide groups on the surface of metallic aluminum is known to decrease with heating under vacuum (40, 41). If the same occurs on the α-Al<sub>2</sub>O<sub>3</sub> surface, one would expect the density of R<sub>s</sub> to decrease. However, this can only occur once sufficient surface water has been removed. This would explain the resistance of R<sub>s</sub> to heating under vacuum. Even so, under ambient conditions, a dehydrated α-Al<sub>2</sub>O<sub>3</sub> surface will likely become rehydrated and rehydroxylated (42) and eventually undergo oxidation by O<sub>2</sub>, leading to the reappearance of R<sub>s</sub> centers.

Chemically more aggressive Ar/O<sub>2</sub> plasma treatment of the α-Al<sub>2</sub>O<sub>3</sub> surface has no initial net effect on R<sub>s</sub>. Nonetheless, the surface is exposed to high concentrations of various oxygen species: O<sub>2</sub>, superoxides (as evidenced by the cESR spectra, Fig. 7), and peroxides that persist on the surface (36). The eventual decrease of the population of R<sub>s</sub> is consistent with shifts in the equilibria in scheme 1 in response to increase superoxide and peroxide concentrations. The importance of this is that the long time scales of these changes indicated that the “silencing” of R<sub>s</sub> can be made essentially irreversible.

From these observations, we conclude that control over R<sub>s</sub> is possible. A step toward more efficient faster passivation of these centers will be to identify which of the plasma-induced species react with R<sub>s</sub> and the underlying mechanism that is involved. It is clear that HFEPR and high magnetic field hyperfine spectroscopy methods used to identify and characterize these centers of noise and decoherence will also provide relatively simple analytical techniques for quantitative step-by-step assessment of strategies for passivating these radical centers, thereby improving the noise characteristics of characteristics of superconducting and quantum devices.

In conclusion, using high-field EPR, ENDOR, and ELDOR-NMR on α-Al<sub>2</sub>O<sub>3</sub> substrates, we have revealed that the radical centers previously associated with noise in superconducting devices rather than being adsorbed species are immanent to the surface. Structural optimization of a DFT model based on an Al<sub>8</sub>O<sub>30</sub>H<sub>36</sub> cluster leads to the formation of specific radicals with calculated hyperfine couplings in good agreement with experiments. Crucially, the surface radicals that we find are very complex entities where the electron spin extends over two nonequivalent Al sites and three different protons, yielding highly complex interactions. DFT calculations allow us to attribute the origin of these exceptionally stable radicals to reactive oxygen chemistry with hydrated surface sites. Such chemistry has been demonstrated to occur on the surface of many oxides of main group and transition metals (22, 24, 25), likely explaining the ubiquity of paramagnetic noise in quantum devices made from a range of different materials. We have shown that HFEPR allows for identification and studies of these surface noise centers in a facile and versatile manner not achievable with other techniques. Hence, it is an invaluable tool for assessing the strategies for passivating these stable radical centers in pursuit to mitigate the noise and decoherence in quantum devices. Our computation results suggest that one important step toward this goal will be to understand oxidation chemistry of the metal oxide surfaces used in engineered quantum devices and quantum-limited sensors.

## MATERIALS AND METHODS

### Samples

Samples were cut from a 50-mm-diameter and 320-μm-thick circular (0001)-cut α-Al<sub>2</sub>O<sub>3</sub> wafer obtained from Shinkosha Co. (Yokohama, Japan). The crystal *c* axis was perpendicular to the surface, and one



cut was made along the crystal  $a$  axis and the other in the perpendicular direction. For EPR measurements at 190 and 285 GHz, the samples were 5 mm by 5 mm by 0.5 mm plates, and for the 94-GHz pulse EPR measurements, a 5 mm by 0.5 mm by 0.5 mm sample with the  $a$  axis along the long direction (fig. S1) was cut from the same single crystal as the larger 5 mm by 5 mm by 0.5 mm samples and used. The crystallographic orientation was verified by x-ray diffraction measurements. The same substrate had also been used for the fabrication of the high-quality NbN superconducting resonators reported in (43), where details of all fabrication steps can be found. Of importance for this study, as a final step, the substrates were annealed at 300°C for 15 min in vacuum ( $10^{-9}$  torr) to remove atomic hydrogen adsorbents.

### EPR measurements

The 190- and 285-GHz EPR spectra were obtained on a constructed HF-EPR spectrometer, which has been previously described (44). The spectra were taken at 4 K using conventional continuous-wave excitation and magnetic field modulation with an amplitude of 0.5 mT and a frequency of 3 kHz. This led to fast-passage saturated line shapes that were absorptive rather than derivative (45). Under these conditions, the contributions of the three  $\alpha$ -Al<sub>2</sub>O<sub>3</sub> radicals to the spectra were expected to be spin relaxation dependent. This apparently enhanced the contribution of  $R_s$ .

The 94-GHz EPR, ELDOR-NMR, and ENDOR spectra were obtained at 50 K with a Bruker Elexsys II 680 EPR spectrometer equipped with an Oxford Instruments CF935 flow cryostat and arbitrary waveform generators ("SpinJet AWG," Bruker). Some spectra were obtained with a locally constructed 2-W 94-GHz microwave bridge based on the design by Nalepa *et al.* (46). The 94-GHz field-swept spin-echo spectra were obtained between 50 and 70 K by monitoring the integrated intensity of the two-pulse Hahn spin echo (fig. S2) as a function of the static applied magnetic field  $B_0$  (30). Spectra were obtained using pulse separation times ( $\tau$ ) of 400 to 500 ns and with  $\pi$  pulse times of 16 to 50 ns. Sufficiently long shot-repetition times of at least 4 ms were used to ensure fully relaxed spectra. Under these conditions, in contrast to the 190- and 285-GHz spectra, the line shapes of the 94-GHz spectra reflected the actual contributions of the  $R_{cl}$ ,  $R_{clb}$ , and  $R_s$ . The decay rate of the echo as a function  $\tau$  is characterized by the phase memory time  $T_m$ . The  $T_m$ -filtered spectra shown in Fig. 2C were obtained by subtracting spectra taken with  $\tau = 10 \mu\text{s}$  from those with  $\tau = 500$  ns. At the longer  $\tau$ , the  $R_s$  contribution was substantially reduced owing to its much faster  $T_m$ . The 94-GHz <sup>1</sup>H Mims ENDOR (47) spectra shown in the Supplementary Materials were obtained in a standard manner with  $\pi$  pulse times of 16 to 50 ns and radio-frequency pulse length of 20  $\mu\text{s}$ . The <sup>27</sup>Al Davies ENDOR (31) spectra were obtained in a similar manner using the same pulse times.

The 94-GHz <sup>1</sup>H ELDOR-NMR (20) spectra were obtained by tuning the microwave cavity to 72 MHz above the detection frequency and overcoupling the cavity. The spectra were acquired by first applying a 30- $\mu\text{s}$  variable frequency pump pulse, followed by a delay of 1  $\mu\text{s}$  and detection using a Hahn echo sequence with  $\tau = 400$  ns and  $\pi$  pulse times of 200 ns. The microwave excitation field was approximately the same for the pump and detection. For the two-spin and three-spin <sup>27</sup>Al ELDOR-NMR spectra, the cavity was tuned to 37 MHz [corresponding to the <sup>27</sup>Al NMR (Zeeman) frequency] above the detection frequency and overcoupled. The three-spin spectra were collected in the same manner as the <sup>1</sup>H ELDOR-NMR

spectrum. For the two-spin spectrum, the AWG was used to generate a 10- $\mu\text{s}$  Gaussian pump pulse and the Hahn echo detection used a  $\tau = 400$  ns and  $\pi$  pulse times of 300 ns. The baselines of these two-spin and three-spin spectra were corrected by fitting them to a quadratic polynomial. The three-spin ELDOR-NMR spectra involving protons were obtained by tuning the overcoupled cavity 100 MHz above the detection frequency. The spectra were taken at 60 K using a 70- to 80- $\mu\text{s}$  pump pulse,  $\tau = 500$  ns, and  $\pi$  pulse times of 200 to 300 ns. The baselines of these spectra were corrected using a linear function. The wide frequency bandwidth required to detect the three-spin transitions involving protons and the low probabilities of these transitions made them challenging to detect, and not all orientations yielded usable spectra. The corresponding two-spin spectra shown in Fig. 5 for comparison were measured using the same conditions as the three-spin data. EPR simulations are described in the Supplementary Materials.

### DFT calculations

DFT calculations were carried out using Gaussian (version 16, revision A.03) (48) and ORCA (49). The former was used to optimize geometries and compute the  $g$  tensors using the B3LYP (50–52)/6-31 + G(D, P) (53) hybrid density functional and basis set and default options. The latter was used to obtain the hyperfine coupling values using the PBE0 (54)/6-31 + G(D, P) (54) hybrid functionals B3LYP for  $g$  tensors and PBE0 for hyperfine tensors in conjunction with Gaussian basis sets. The calculations were tested on aluminum radical centers for which the spin interactions have been measured (see the Supplementary Materials). These included stable neutral alumi radicals (55), aluminum dicarbonyl (56), AlH<sup>+</sup> (57), and aluminum ethylene (58). As can be seen from table S1, the calculated  $g$  and hyperfine values for these simple aluminum molecules were in reasonable agreement with those measured.

The Al<sub>8</sub>O<sub>30</sub>H<sub>36</sub> nanoparticle models were based on Al<sub>8</sub>O<sub>30</sub> unit cell. On the basis of experimental studies of the water- $\alpha$ -Al<sub>2</sub>O<sub>3</sub> interface (35), oxygens were added to the exposed aluminum atoms of the Al<sub>8</sub>O<sub>30</sub> core so that each had a complete ligand sphere of six oxygens. Hydrogen atoms were added to all oxygen atoms bridging two aluminum atoms. Another set of hydrogens was added in a quasi-random manner to the rest of the oxygens to form structures with overall neutral charges, resulting in nanoparticles of the form Al<sub>8</sub>O<sub>30</sub>H<sub>36</sub>. These structures were subsequently geometry optimized. To these optimized structures, an O<sub>2</sub> molecule was added and positioned within hydrogen bonding distance of the Al<sub>8</sub>O<sub>30</sub>H<sub>36</sub> model, typically about 1.8 Å. These supermolecular complexes were re-geometry optimized with a total spin multiplicity of 1. Calculations were also carried out on various reduced and oxidized forms of the nanoparticle.

### SUPPLEMENTARY MATERIALS

Supplementary material for this article is available at <https://science.org/doi/10.1126/sciadv.abm6169>

### REFERENCES AND NOTES

1. C. M. Quintana, Y. Chen, D. Sank, A. G. Petukhov, T. C. White, D. Kafri, B. Chiaro, A. Migrant, R. Barends, B. Campbell, Z. Chen, A. Dunsworth, A. G. Fowler, R. Graff, E. Jeffrey, J. Kelly, E. Lucero, J. Y. Mutus, M. Neeley, C. Neill, P. J. J. O'Malley, P. Roushan, A. Shabani, V. N. Smelyanskiy, A. Vainsencher, J. Wenner, H. Neven, J. M. Martinis, Observation of classical-quantum crossover of 1/f Flux noise and its paramagnetic temperature dependence. *Phys. Rev. Lett.* **118**, 057702 (2017).



2. T. Lanting, M. H. Amin, C. Baron, M. Babcock, J. Boschee, S. Boixo, V. N. Smelyanskiy, M. Foygel, A. G. Petukhov, Probing environmental spin polarization with superconducting flux qubits (2020); <https://arxiv.org/abs/2003.14244>.
3. S. Sendelbach, D. Hover, A. Kittel, M. Mück, J. M. Martinis, R. McDermott, Magnetism in SQUIDs at Millikelvin temperatures. *Phys. Rev. Lett.* **100**, 227006 (2008).
4. E. Paladino, Y. Galperin, G. Falci, B. L. Altshuler,  $1/f$  noise: Implications for solid-state quantum information. *Rev. Mod. Phys.* **86**, 361–418 (2014).
5. C. Müller, J. H. Cole, J. Lisenfeld, Towards understanding two-level-systems in amorphous solids: Insights from quantum circuits. *Reports Prog. Phys.* **82**, 124501 (2019).
6. M. R. Vissers, J. E. Austermann, M. Malnou, C. M. McKenney, B. Dober, J. Hubmayr, G. C. Hilton, J. N. Ullom, J. Gao, Ultra-stable millimeter-wave kinetic inductance detectors. *Appl. Phys. Lett.* **116**, 032601 (2020).
7. Y. Romach, C. Müller, T. Uden, L. J. Rogers, T. Isoda, K. M. Itoh, M. Markham, A. Stacey, J. Meijer, S. Pezzagna, B. Naydenov, L. P. McGuinness, N. Bar-Gill, F. Jelezko, Spectroscopy of surface-induced noise using shallow spins in diamond. *Phys. Rev. Lett.* **114**, 017601 (2015).
8. T. Rosskopf, A. Dussaux, K. Ohashi, M. Loretz, R. Schirhagl, H. Watanabe, S. Shikata, K. M. Itoh, C. L. Degen, Investigation of surface magnetic noise by shallow spins in diamond. *Phys. Rev. Lett.* **112**, 147602 (2014).
9. J. Wu, C. C. Yu, Modeling flux noise in SQUIDs due to hyperfine interactions. *Phys. Rev. Lett.* **108**, 247001 (2012).
10. A. De,  $1/f$  flux noise in low- $T_c$  SQUIDs due to superparamagnetic phase transitions in defect clusters. *Phys. Rev. B*, **99**, 024305 (2019).
11. T. Lanting, M. H. Amin, A. J. Berkley, C. Rich, S. F. Chen, S. Laforest, R. De Sousa, Evidence for temperature-dependent spin diffusion as a mechanism of intrinsic flux noise in SQUIDs. *Phys. Rev. B Condens. Matter Mater. Phys.* **89**, 014503 (2014).
12. L. Faoro, L. B. Ioffe, Microscopic origin of low-frequency flux noise in Josephson circuits. *Phys. Rev. Lett.* **100**, 227005 (2008).
13. H. Wang, C. Shi, J. Hu, S. Han, C. C. Yu, R. Q. Wu, Candidate source of flux noise in SQUIDs: Adsorbed oxygen molecules. *Phys. Rev. Lett.* **115**, 077002 (2015).
14. Z. Wang, H. Wang, C. C. Yu, R. Q. Wu, Hydrogen as a source of flux noise in SQUIDs. *Phys. Rev. B*, **98**, 020403 (2018).
15. F. C. Wellstood, C. Urbina, J. Clarke, Low-frequency noise in dc superconducting quantum interference devices below 1 K. *Appl. Phys. Lett.* **50**, 772–774 (1987).
16. H. Bluhm, J. A. Bert, N. C. Koshnick, M. E. Huber, K. A. Moler, Spinlike susceptibility of metallic and insulating thin films at low temperature. *Phys. Rev. Lett.* **103**, 026805 (2009).
17. J. Braumüller, L. Ding, A. P. Vepsäläinen, Y. Sung, M. Kjaergaard, T. Menke, R. Winik, D. Kim, B. M. Niedzielski, A. Melville, J. L. Yoder, C. F. Hirjibehedin, T. P. Orlando, S. Gustavsson, W. D. Oliver, Characterizing and optimizing qubit coherence based on SQUID geometry. *Phys. Rev. Appl.* **13**, 054079 (2020).
18. S. E. De Graaf, A. A. Adamyan, T. Lindström, D. Erts, S. E. Kubatkin, A. Y. Tzalenchuk, A. V. Danilov, Direct identification of dilute surface spins on  $\text{Al}_2\text{O}_3$ : Origin of flux noise in quantum circuits. *Phys. Rev. Lett.* **118**, 057703 (2017).
19. R. A. Marcus, N. Sutin, Electron transfers in chemistry and biology. *BBA Rev. Bioenerg.* **811**, 265–322 (1985).
20. P. Schosseler, T. Wacker, A. Schweiger, Pulsed ELDOR detected NMR. *Chem. Phys. Lett.* **224**, 319–324 (1994).
21. P. Kumar, S. Sendelbach, M. A. A. Beck, J. W. W. Freeland, Z. Wang, H. Wang, C. C. Yu, R. Q. Q. Wu, D. P. P. P. Pappas, R. McDermott, Origin and reduction of  $1/f$  magnetic flux noise in superconducting devices. *Phys. Rev. Appl.* **6**, 041001 (2016).
22. M. Che, A. J. Tench, Characterization and reactivity of molecular oxygen species on oxide surfaces. *Adv. Catal.* **32**, 1–148 (1983).
23. M. Anpo, M. Che, B. Fubini, E. Garrone, E. Giannelo, M. C. Paganini, Generation of superoxide ions at oxide surfaces. *Top. Catal.* **8**, 189–198 (1999).
24. A. Gurlo, Interplay between  $\text{O}_2$  and  $\text{SnO}_2$ : Oxygen ionosorption and spectroscopic evidence for adsorbed oxygen. *ChemPhysChem* **7**, 2041–2052 (2006).
25. K. Sobaińska, A. Krasowska, T. Mazur, K. Podolska-Serafin, P. Pietrzyk, Z. Sojka, Diagnostic features of EPR spectra of superoxide intermediates on catalytic surfaces and molecular interpretation of their G and A tensors. *Top. Catal.* **58**, 796–810 (2015).
26. D. A. Medvedev, A. A. Rybinskaya, R. M. Kenzhin, A. M. Volodin, A. F. Bedilo, Characterization of electron donor sites on  $\text{Al}_2\text{O}_3$  surface. *Phys. Chem. Chem. Phys.* **14**, 2587–2598 (2012).
27. D. B. Losee, The stabilization of  $\text{O}_2^-$  on  $\gamma\text{-Al}_2\text{O}_3$ . *J. Catal.* **50**, 545–548 (1977).
28. J. H. Lunsford, L. W. Zingery, M. P. Rosynek, Exposed aluminum ions as active sites on  $\gamma$ -alumina. *J. Catal.* **38**, 179–188 (1975).
29. P. Krantz, M. Kjaergaard, F. Yan, T. P. Orlando, S. Gustavsson, W. D. Oliver, A quantum engineer's guide to superconducting qubits. *Appl. Phys. Rev.* **6**, 21318 (2019).
30. E. L. Hahn, Spin echoes. *Phys. Rev.* **80**, 580–594 (1950).
31. E. R. Davies, A new pulse endor technique. *Phys. Lett. A*, **47**, 1–2 (1974).
32. M. Haouas, F. Taulelle, C. Martineau, Recent advances in application of  $^{27}\text{Al}$  NMR spectroscopy to materials science. *Prog. Nucl. Magn. Reson. Spectrosc.* **94–95**, 11–36 (2016).
33. S. Sendelbach, D. Hover, M. Mück, R. McDermott, Complex inductance, excess noise, and surface magnetism in dc SQUIDs. *Phys. Rev. Lett.* **103**, 117001 (2009).
34. S. E. De Graaf, L. Faoro, J. Burnett, A. A. Adamyan, A. Y. Tzalenchuk, S. E. Kubatkin, T. Lindström, A. V. Danilov, Suppression of low-frequency charge noise in superconducting resonators by surface spin desorption. *Nat. Commun.* **9**, 1–6 (2018).
35. J. G. Catalano, C. Park, Z. Zhang, P. Fenter, Termination and water adsorption at the  $\alpha\text{-Al}_2\text{O}_3(012)$ –Aqueous solution interface. *Langmuir* **22**, 4668–4673 (2006).
36. T. Takamatsu, K. Uehara, Y. Sasaki, H. Miyahara, Y. Matsumura, A. Iwasawa, N. Ito, T. Azuma, M. Kohno, A. Okino, Investigation of reactive species using various gas plasmas. *RSC Adv.* **4**, 39901–39905 (2014).
37. B. H. J. Bielski, D. E. Cabelli, *Active Oxygen in Chemistry* (Springer Netherlands, 1995; [https://link.springer.com/chapter/10.1007/978-94-007-0874-7\\_3](https://link.springer.com/chapter/10.1007/978-94-007-0874-7_3)), pp. 66–104.
38. L. A. Pardi, J. Krzystek, J. Telsler, L. C. Brunel, Multifrequency EPR spectra of molecular oxygen in solid air. *J. Magn. Reson.* **146**, 375–378 (2000).
39. B. H. J. Bielski, A. O. Allen, Mechanism of the disproportionation of superoxide radicals. *J. Phys. Chem.* **81**, 1048–1050 (1977).
40. A. Nylund, I. Olejford, Surface analysis of oxidized aluminium. 1. Hydration of  $\text{Al}_2\text{O}_3$  and decomposition of  $\text{Al}(\text{OH})_3$  in a vacuum as studied by ESCA. *Surf. Interface Anal.* **21**, 283–289 (1994).
41. M. R. Alexander, G. E. Thompson, G. Beamson, Characterization of the oxide/hydroxide surface of aluminium using X-ray photoelectron spectroscopy: A procedure for curve fitting the O 1s core level. *Surf. Interface Anal.* **29**, 468–477 (2000).
42. P. J. Eng, T. P. Trainor, G. E. Brown, G. A. Waychunas, M. Newville, S. R. Sutton, M. L. Rivers, Structure of the hydrated  $\alpha\text{-Al}_2\text{O}_3$  (0001) surface. *Science* **288**, 1029–1033 (2000).
43. S. Mahashabde, E. Otto, D. Montemurro, S. De Graaf, S. Kubatkin, A. Danilov, Fast tunable high-Q-factor superconducting microwave resonators. *Phys. Rev. Appl.* **14**, 44040 (2020).
44. S. Un, P. Dorlet, A. W. Rutherford, A high-field EPR tour of radicals in photosystems I and II. *Appl. Magn. Reson.* **21**, 341–361 (2001).
45. M. Weger, Passage effects in paramagnetic resonance experiments. *Bell Syst. Tech. J.* **39**, 1013–1112 (1960).
46. A. Nalepa, K. Möbius, W. Lubitz, A. Savitsky, High-field ELDOR-detected NMR study of a nitroxide radical in disordered solids: Towards characterization of heterogeneity of microenvironments in spin-labeled systems. *J. Magn. Reson.* **242**, 203–213 (2014).
47. W. B. Mims, Pulsed endor experiments. *Proc. R. Soc. Lond. A. Math. Phys. Sci.* **283**, 452–457 (1965).
48. M. J. Frisch, G. W. Trucks, H. B. Schlegel, G. E. Scuseria, M. A. Robb, J. R. Cheeseman, G. Scalmani, V. Barone, G. A. Petersson, H. Nakatsuji, X. Li, M. Caricato, A. V. Marenich, J. Bloino, B. G. Janesko, R. Gomperts, B. Mennucci, H. P. Hratchian, J. V. Ortiz, A. F. Izmaylov, J. L. Sonnenberg, D. Williams-Young, F. Ding, F. Lipparini, F. Egidi, J. Goings, B. Peng, A. Petrone, T. Henderson, D. Ranasinghe, V. G. Zakrzewski, J. Gao, N. Rega, G. Zheng, W. Liang, M. Hada, M. Ehara, K. Toyota, R. Fukuda, J. Hasegawa, M. Ishida, T. Nakajima, Y. Honda, O. Kitao, H. Nakai, T. Vreven, K. Throssell, J. A. Montgomery Jr., J. E. Peralta, F. Ogliaro, M. J. Bearpark, J. J. Heyd, E. N. Brothers, K. N. Kudin, V. N. Staroverov, T. A. Keith, R. Kobayashi, J. Normand, K. Raghavachari, A. P. Rendell, J. C. Burant, S. S. Iyengar, J. Tomasi, M. Cossi, J. M. Millam, M. Klene, C. Adamo, R. Cammi, J. W. Ochterski, R. L. Martin, K. Morokuma, O. Farkas, J. B. Foresman, D. J. Fox, Gaussian 16 Revision A.03 (2016).
49. F. Neese, The ORCA program system. *Wiley Interdiscip. Rev. Comput. Mol. Sci.* **2**, 73–78 (2012).
50. A. D. Becke, Density-functional exchange-energy approximation with correct asymptotic behavior. *Phys. Rev. A* **38**, 3098–3100 (1988).
51. C. Lee, W. Yang, R. G. Parr, Development of the Colle-Salvetti correlation-energy formula into a functional of the electron density. *Phys. Rev. B*, **37**, 785–789 (1988).
52. A. D. Becke, A new mixing of Hartree-Fock and local density-functional theories. *J. Chem. Phys.* **98**, 1372–1377 (1993).
53. V. A. Rassolov, J. A. Pople, M. A. Ratner, T. L. Windus, 6-31G\* basis set for atoms K through Zn. *J. Chem. Phys.* **109**, 1223–1229 (1998).
54. C. Adamo, V. Barone, Toward reliable density functional methods without adjustable parameters: The PBE0 model. *J. Chem. Phys.* **110**, 6158 (1999).
55. B. Li, S. Kundu, A. C. Stückli, H. Zhu, H. Keil, R. Herbst-Irmer, D. Stalke, B. Schwederski, W. Kaim, D. M. Andradá, G. Frenking, H. W. Roesky, A stable neutral radical in the coordination sphere of aluminum. *Angew. Chemie Int. Ed.* **56**, 397–400 (2017).
56. P. H. Kasai, P. M. Jones, Aluminum dicarbonyl: Matrix isolation ESR study. *J. Am. Chem. Soc.* **106**, 8018–8020 (1984).
57. L. B. Knight, E. Earl, A. R. Ligon, D. P. Cobranchi, J. R. Woodward, J. M. Bostick, E. R. Davidson, D. Feller, Neon matrix ESR and CI theoretical investigation of  $\text{AlF}^+$ ; photoionization of  $\text{AlF}$  from thermal and laser sputtering generation methods. *J. Am. Chem. Soc.* **108**, 5065–5071 (1986).
58. P. H. Kasai, Aluminum atom-ethylene and aluminum atom-acetylene complexes: Matrix isolation electron spin resonance study. *J. Am. Chem. Soc.* **104**, 1165–1172 (1982).

59. A. Schweiger, G. Jeschke, *Principles of Pulse Electron Paramagnetic Resonance* (Oxford Univ. Press, 2001).

#### Acknowledgments

**Funding:** S.U. acknowledges the Biophysics Platform of the Institute for Integrative Biology of the Cell supported by French Infrastructure for Integrated Structural Biology (FRISBI, grant ANR-10-INBS-05-05). This work was supported by U.K. government Department for Business, Energy and Industrial Strategy through the U.K. National Quantum Technologies Programme (S.d.G.); Swedish Research Council (VR) grants 016-04828 and 2019-05480 (S.K. and A.D.); Knut and Alice Wallenberg Foundation via the Wallenberg Center for Quantum Technology (WACQT); EU H2020 European Microkelvin Platform grant 824109 (S.K. and A.D.); CEA DRF-Impulsion Program (P.B.

and S.U.); and DIM-ELICIT and SESAME programs of the Région Ile-de-France. (S.U.).

**Author contributions:** Conceptualization: S.U., S.d.G., A.D., S.K., and P.B. Methodology: S.U. Investigation: S.U., S.d.G., S.D., and S.K. Writing—original draft: S.U., S.d.G., and A.D. Writing—review and editing: S.U., S.d.G., A.D., S.K., and P.B. **Competing interests:** The authors declare that they have no competing interests. **Data and materials availability:** All data needed to evaluate the conclusions in the paper are present in the paper and/or the Supplementary Materials.

Submitted 6 October 2021

Accepted 11 February 2022

Published 6 April 2022

10.1126/sciadv.abm6169